

Article

# Numerical Simulation on Supercritical CO<sub>2</sub> Fluid Dynamics in a Hollow Fiber Membrane Contactor

Hugo Valdés <sup>1,\*</sup> , Kevin Unda <sup>2</sup> and Aldo Saavedra <sup>3</sup>

<sup>1</sup> Centro de Innovación en Ingeniería Aplicada, Departamento de Computación e Industrias, Universidad Católica del Maule, Avda. San Miguel 3605, Talca, Chile

<sup>2</sup> Departamento de Obras Civiles, Universidad Católica del Maule, Avda. San Miguel 3605, Talca, Chile; keundaf@gmail.com

<sup>3</sup> Departamento de Ingeniería Química, Universidad de Santiago de Chile, Avda. Libertador Bernardo O'Higgins 3303, Santiago, Chile; aldo.saavedra@usach.cl

\* Correspondence: hugo.vr@gmail.com or hvaldes@ucm.cl; Tel.: +56-71-2203541

Received: 27 November 2018; Accepted: 10 January 2019; Published: 15 January 2019



**Abstract:** This research answers the following question: What is the fluid dynamic behavior of a supercritical fluid (SCF) inside a membrane module? At this time, there is very little or no reported information that can provide an answer to this question. The research studies related to the themes of supercritical CO<sub>2</sub> (SC-CO<sub>2</sub>), hollow fiber membrane contactors (HFMCs), and numerical simulations have mainly reported on 2D simulations, but in this work, 3D profiles are presented. Simulations were performed based on the experimental results and other simulations, using the geometry of a commercial module. The results were mainly based on the different operating conditions and geometric dimensions. A mesh study was performed to ensure the mesh non-dependence of the results presented here. It was observed that the velocity profile developed at 10 mm from the wall of the supercritical CO<sub>2</sub> entrance pipe. A profile equilibrium around the fiber close to the entrance of the module was achieved in the experimental hollow fiber membrane contactor when compared to the case of the commercial hollow fiber membrane contactor. The results of this research provided a visualization of the boundary layer, which did not cover the entire fiber length. Finally, the results of this paper are interesting for technical applications and contribute to our understanding of the hydrodynamics of SCFs.

**Keywords:** numerical simulation; fluid dynamics; supercritical CO<sub>2</sub>; membrane contactor

## 1. Introduction

Each year, the number of research studies related to the themes of supercritical CO<sub>2</sub> (SC-CO<sub>2</sub>), hollow fiber membrane contactors (HFMCs) and numerical simulations are increasing (see Figure 1). Researchers have mainly reported on the 2D simulations of the mass transfer and velocity profile [1–4], however, the question of what the fluid dynamic behavior of a supercritical fluid (SCF) is inside a membrane module still remains.

Membranes are semi-permeable barriers capable of separating substances by means of various mechanisms (solution/diffusion, Knudsen diffusion, molecular sieving, and ion transport). They are available in different types of materials: Organic (polymeric) or inorganic (carbon, zeolite, ceramic, or metallic), and may or may not be porous [5]. The membranes act as filters that separate one or more compounds from a feed mixture and generate a permeate phase rich in the specific compound [6]. Microporous hollow fiber modules provide a larger contact area per volume between gas and liquid than conventional devices [7]. In the hollow fiber membrane contactors, the gas mixture flows on one side of a microporous membrane, while the liquid absorbent flows on the other side. A gas–liquid

interface forms at the opening adjacent to the liquid absorbent when the membrane is not wet with liquid, but filled with gas (Figure 2). In the absorption process based on microporous hollow fibers, gases diffuse from the gas phase to the gas–liquid interface through the pores and are absorbed in the liquid solvent [8]. Compared to conventional devices including the packed tower, spray tower, venturi scrubber, and bubble column, the hollow fiber membrane contactor has the following advantages [9] of operational flexibility, greater economy, linear scale-up, and easier performance prediction.

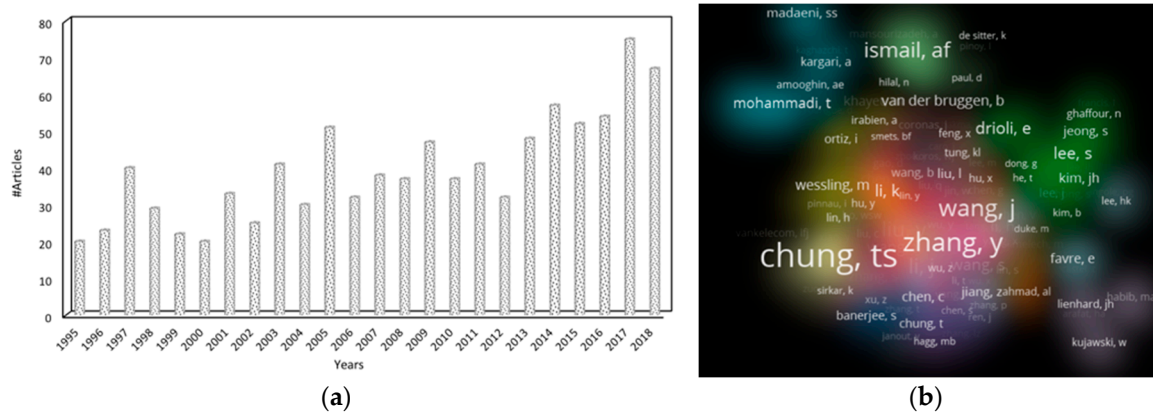


**Figure 1.** (a) Published papers on the ScienceDirect website from 1995 until 2018. Advanced search: “Numerical simulation” + “membrane” + “supercritical”; (b) density visualization (VOSviewer) of authors (with co-citation) for “membrane” + “simulation” + “hollow fiber” in Web of Science.

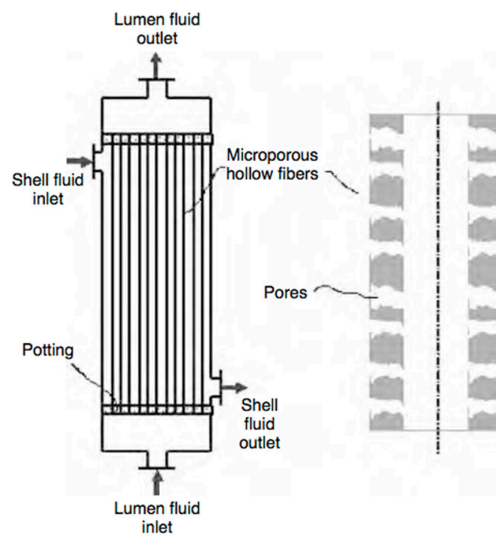


**Figure 2.** Porous hollow fiber membrane in a membrane contactor [10].

On the other hand, a fluid is supercritical when its temperature and pressure are greater than its critical point values ( $T_C$ ,  $P_C$ ). Most applications of SCFs occur in the range of  $1 < T/T_C < 1.1$  and  $1 < P/P_C < 2$  [11]. Under these conditions, the fluid exists as a single phase with some of the advantageous properties of both a liquid and a gas: It has sufficient density to provide appreciable dissolving power; but the diffusivity of solutes in SCFs is higher than in liquids, and the viscosity of SCFs is lower, facilitating mass transport and endowing SCFs with more favorable hydrodynamic properties than those of the liquids. Finally, due to the high compressibility of fluids near the critical point, their density and dissolving power can be tuned sensitively through small changes in pressure [12]. Furthermore, solute solubility depends exponentially on density [13], and small pressure changes in the highly compressible critical region can cause very large solubility variations, allowing the selective dissolution

or precipitation of solutes [12,14]. On the other hand, their very low surface tension allows them to penetrate readily porous solids and packed beds [15].

The thermodynamic properties of the fluid at the critical point have their theoretical basis in that the first and second partial derivatives of the pressure, with respect to the volume at a constant temperature  $T_C$ , are zero because there is a point of inflection at the critical point. This implies that, at the critical point, the isothermal compressibility and the coefficient of the thermal expansion are infinitely positive, the enthalpy of vaporization is zero, and the specific heat at a constant volume is infinite.

For the hydrodynamic analysis, it is necessary to know the behavior of the density and viscosity in the vicinity of the critical point. Density in the supercritical region increases sharply with increasing pressure at a constant temperature; in addition, it decreases with increasing temperature at a constant pressure. It is worth emphasizing the steep slopes of the curves in the vicinity of the critical point [14,16]. As reported by Stephan [17], at constant pressure, viscosity under subcritical conditions ( $T < T_C$ ) decreases with increasing temperature to the critical point, then viscosity under supercritical conditions ( $T > T_C$ ) increases with increasing temperature. In SCFs, viscosity increases with the pressure at a constant temperature. In general, the influence of pressure is low at high reduced temperatures ( $T/T_C$ ) and at low reduced pressures ( $P/P_C$ ) [18]. Moreover, increased pressures also result in diminished solute diffusivity and transport phenomena, but also in increased solubility through decreased density [18].

The main compound used under critical and supercritical conditions is  $\text{CO}_2$ . Until 2018, 27,233 journals on SC- $\text{CO}_2$  applications had been published on the ScienceDirect website [19–28]. The broad use of SC- $\text{CO}_2$  is due to the fact that it is inexpensive, chemically inert, non-toxic, and non-flammable, has a relatively low critical point ( $P_C = 7.38$  MPa,  $T_C = 304.15$  K), and is considered by the Food and Drug Administration (FDA) as being a GRAS (Generally Recognized as Safe) product [29].

Pabby and Sastre [30] reported that a particularly interesting application of membrane contactors is extraction with dense gases (i.e., near critical or SCFs). Like liquids, dense gases offer the high solubility of many solutes of interest, yet also offer the high mass transfer rate and low pressure drop enjoyed with gases. Furthermore, solubility is usually a strong function of density, and dense gas is thus easily separated from the dissolved solutes simply by reducing the pressure [31,32]. Due to the growing interest in SC- $\text{CO}_2$  applications, one of them being in membrane contactors, this paper presents the fluid dynamic behavior of the SC- $\text{CO}_2$  for different configurations of hollow fiber membrane modules. The authors highlight that this research helps to visualize the velocity profiles, the formation of the boundary layer, the effects of geometry, among other aspects, which supports the accuracy of models to determine the phenomena of material transference.

### *Supercritical $\text{CO}_2$ in a Membrane Contactor*

The method that takes into account the use of SCFs in a membrane contactor is called the Porocrit process (PoroCrit LLC, Berkeley, CA, USA) [33]. It is different from the traditional membrane processes based on the pressure difference since in the case of the Porocrit membrane process, it is porous and acts mainly as a contact device that allows the stabilization of an interface between two phases of matter exchange, the feeding solution, and the SC- $\text{CO}_2$  extraction solvent [34].

The membrane contactors used in the Porocrit process are of the hollow fiber type. Several studies have considered the use of SC- $\text{CO}_2$  in hollow fiber membrane contactors (HFMCs) [19,34–42]. There are two important issues for the Porocrit process: The mass transfer (MT) and fluid dynamics (FD) inside the membrane module. Much of the research based on the Porocrit process is focused on the MT, whereas this research work focuses on the other important issue, the FD.

In the research on the MT in HFMCs, the following is assumed: A steady-state system; equilibrium is reached at the fluid–fluid interface; the phases present in the shell and tubes are perfectly mixed; there is a developed laminar flow; the pore size is uniform in the whole membrane; the curvature of the interface does not have a significant effect on the mass transfer or solute distribution; the membrane

is “humidified” homogeneously; the mass transfer is correctly described with the boundary layer model; MT does not occur in the non-porous zone of the membrane; the fluids are immiscible; and the coefficient of the partition of the solute is constant [43–50]. On the other hand, there are authors that have studied the MT in HFMCs that have used SC-CO<sub>2</sub> as a solvent [1,19,43,51–53].

This research study’s purpose is to deepen the understanding of the fluid dynamic behavior of an SCF inside a membrane module.

## 2. Materials and Methods

The methodology is outlined in Figure 3. In the initial stage, the experiments performed by Valdés and collaborators [19] were analyzed as these experiments considered the passage of the SC-CO<sub>2</sub> through the shell of the HFMC. Then, the following problem was established: There is uncertainty regarding the fluid dynamic behavior of the SC-CO<sub>2</sub> inside the HFMC. Hence, three cases (A, B, and C) were defined to solve this assumption. In both cases, the FD simulations were performed under the experimental operating conditions reported by Valdés et al. [19], along with the variation of the number of fibers. Case A considered the HFMC manufactured by Valdés and collaborators [19], whereas Case B considered the dimensions of a commercial HFMC with the dimensions of the Case A fiber, and Case C was the commercial HFMC with the fiber dimensions given for this module. In the cases studied in this research, the change in pressure and temperature along the membrane was negligible and imperceptible. Subsequently, the simulations were performed with the Computational Fluid Dynamics (CFD) tool of the ANSYS software. Finally, the results obtained were analyzed.

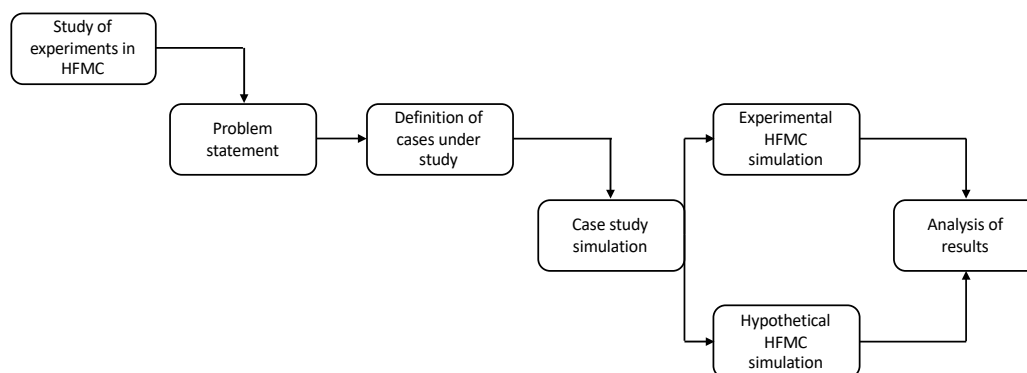


**Figure 3.** Outline of the methodology followed in this research work.

The conservation equations were solved using ANSYS/FLUENT applications and numeric libraries. These apply the finite volume method to unstructured meshes of polyhedral elements by using a spatial discretization scheme in the cell centers. The time discretization was implicitly performed, treating the pressure-velocity coupling in an analogous manner to what is described by Rhie and Chow [54].

### 2.1. Experimental System

The FD simulations were based on three cases: A, B, and C. Case A considered the experimental operating conditions (Table 1) of Valdés et al. [19]. This research work was based on the experimental methodology of the Porocrit process. The authors ran experiments with HFMC manufactured by them.

On the other hand, Cases B and C considered that the dimensions of the commercial HFMC (MiniModule™, Liquicel, 13840 South Lakes Dr. Charlotte, NC 28273 USA) had a pore size of 0.3 μm, wall thickness (fiber) of 0.04 mm, active length of 0.114 m, internal diameter of shell of 42.5 mm, and the outside fiber diameters were 1.8 and 0.3 mm for Cases B and C, respectively (Figure 4). For these geometries, the operating conditions of the HFMC manufactured by the authors were considered. The simulation of Cases B and C allowed us to project future studies.

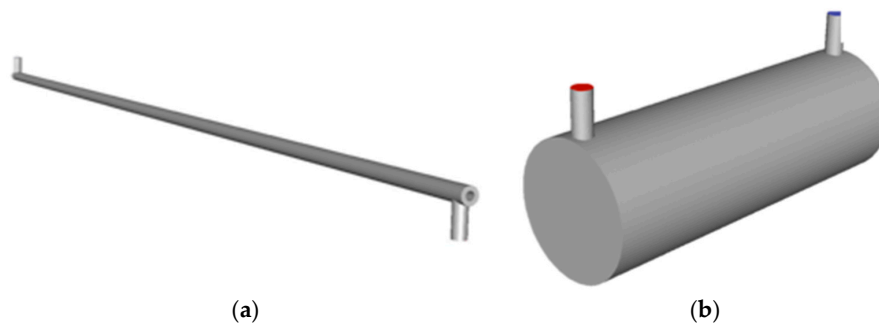


**Figure 4.** (a) Geometry experimental case A; (b) geometry commercial hollow fiber membrane contactor (HFMC) case (B and C).

**Table 1.** Summary of the experimental operating conditions [19].

Property (SC-CO <sub>2</sub> )	Pressure: 90 bar	Pressure: 70 bar	Unit
Density	483.81	198.19	kg m <sup>-3</sup>
Viscosity	3.615 × 10 <sup>-5</sup>	2.017 × 10 <sup>-5</sup>	kg m <sup>-1</sup> s <sup>-1</sup>
Velocity range (inlet)	(2.48–5.57) × 10 <sup>-4</sup>	(6.04–13.60) × 10 <sup>-4</sup>	m s <sup>-1</sup>
Temperature	40	40	°C
Features of the HFMC (PTFE-Fiber)			Unit
Outside diameter (fiber)	1.8		mm
Wall thickness (fiber)	0.4		mm
Active length (fiber)	0.353		m
Number of fibers	1		-
Internal diameter (shell)	3.6		mm
Pore size	2.0		µm

### 2.2. Numerical Method

The behavior of the fluids in motion was of interest to us as well as the way in which it related to the moments and forces applied. Both liquids and gases have a different way of behaving when they are subjected to tangential stresses, which explains their fluidity and why they are crucial in developing the principles of FD.

FD has its fundamental basis on conservation equations, i.e., in the cases studied, it was considered as an incompressible flow, which is why the density remained constant. Thus, the conservation equation of the mass is as follows:

$$\frac{\partial u_i}{\partial x_i} = 0, \tag{1}$$

where  $u_i$  and  $x_i$  are the velocity and the distance components, respectively. On the other hand, there are conservation momentum equations. It is expected that at some point, the flow reaches a steady state, thus the velocity does not change over time, resulting in the following:

$$\rho \frac{\partial u_j u_i}{\partial x_j} = \frac{\partial \tau_{ji}}{\partial x_j} - \frac{\partial p}{\partial x_i}, \tag{2}$$

where  $\tau_{ji}$  represents the components of the shear stress tensor; and  $\rho$  and  $p$  are the density and pressure of the system, respectively. The gravity effect is not considered.

Due to the complexity that turbulent movements can have, as reported by Ferziger and Peić [55], it has become necessary to have simplified models to describe the physical phenomena. The most common of these is the Reynold’s Averaged Navier–Stokes equation (RANS), with which the equation for the conservation of momentum is as follows:

$$\rho \frac{\partial \overline{u_j u_i}}{\partial x_j} = - \frac{\partial \overline{p}}{\partial x_i} + \frac{\partial \overline{\tau_{ji}}}{\partial x_j} - \rho \frac{\partial \overline{u_j' u_i'}}{\partial x_j}, \tag{3}$$

where the last term of the previous equation  $-\rho \overline{u_j' u_i'}$  is called the Reynolds stress, which cannot be calculated directly; therefore, turbulence models are required to obtain an approximation of their value. In this research, the RSM turbulence model was used to obtain these Reynolds tensions.

This model calculated a transport equation separately for each Reynolds stress, thus abandoning the hypothesis of the fluid’s isotropic behavior and therefore being able to show the curvature of the streamlines and the rapid changes in the strain rate tensor, which were expected to be found in the case studies. There are low-Reynolds turbulence models [56], which allow a good approximation within the vicinity of the fiber wall. Since the number of Reynolds in the shell of a membrane module is very low ( $8 < Re < 20$ ), the velocity profile in the boundary layer is expected to be very abrupt; therefore, a significant refinement of the mesh in the vicinity of the wall is necessary for the model to satisfactorily comply with the study requirements.

The transport equations of the Reynolds efforts have the following form:

$$\frac{\partial \overline{u_k} \tau_{ij}}{\partial x_k} = - \left( \tau_{ik} \frac{\partial \overline{u_j}}{\partial x_k} + \tau_{jk} \frac{\partial \overline{u_i}}{\partial x_k} \right) + \rho \varepsilon_{ij} - \Pi_{ij} + \frac{\partial}{\partial x_k} \left( \nu \frac{\partial \tau_{ij}}{\partial x_k} + C_{ijk} \right) + S, \tag{4}$$

where the transport equation is defined for  $\tau_{ij} = \overline{\rho u_j' u_i'}$  and is composed of strength production terms (first two terms), dissipation tensor ( $\rho \varepsilon_{ij}$ ), pressure-strain ( $\Pi_{ij}$ ), two diffusion terms: Molecular ( $\nu \frac{\partial \tau_{ij}}{\partial x_k}$ ) and turbulent ( $C_{ijk}$ ), and in addition, a source tensor ( $S$ ) that can be defined by the user. For the dissipation and pressure-strain tensors, modeling is required in order for them to be calculated. The RSM model models the dissipation as isotropic and in the cases used, a linear model was used for the pressure-strain.

The turbulent model was used instead of the laminar model because of the low Reynolds number. Laminar models in computational fluid dynamics tend to be unstable at this range of velocity and diverge easily at minimal instability. Figure 5 also shows that turbulent phenomena were expected given the order of magnitude of turbulent viscosity giving more problems for the laminar model to converge. A decrease in the turbulent viscosity profile at the entrance to the HFMC was observed as the number of fibers increased. In this case, the number of fibers was as follows: 0, 4, 17, and 25.

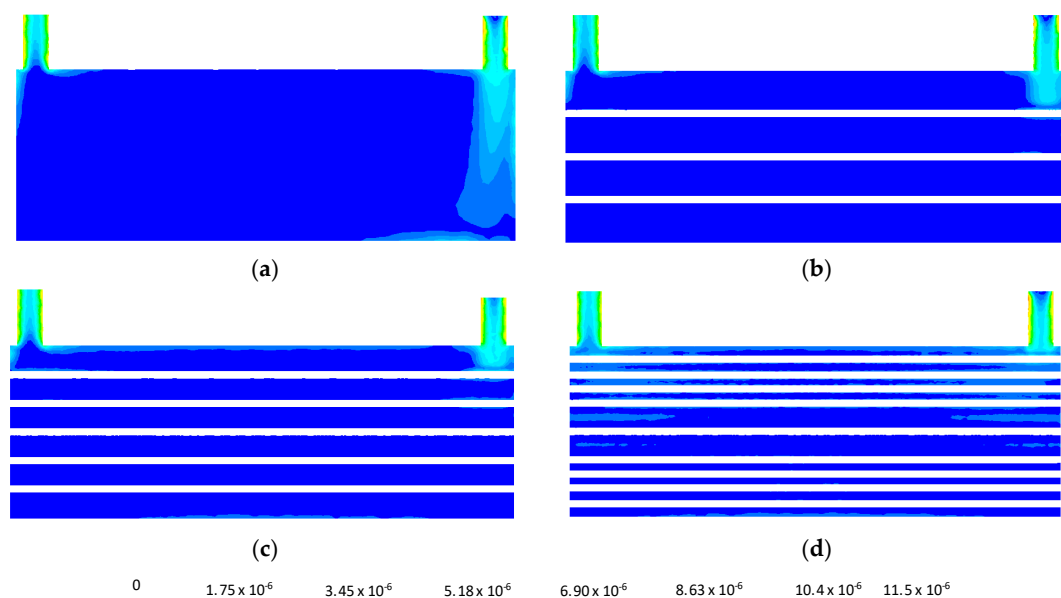


**Figure 5.** Turbulent viscosity in hollow fiber membrane contactors (HFMC) (2D), according to the number of fibers: (a) 0; (b) 4; (c) 17; and (d) 25.

Table 2 summarizes the cases that will be analyzed with the FD simulation. In Cases A, B, and C, as described above, the speed of the experiments of Valdés et al. [19] was used with these values.

**Table 2.** List of the cases analyzed.

Case	Pressure (bar)	Velocity $\times 10^4$ (m/s)	Number of Fibers
A.1	70	6.0445	1
A.2		7.5557	
A.3		9.0668	
A.4		10.5779	
A.5		12.0891	
A.6		13.6002	
A.7	90	2.4761	
A.8		3.0951	
A.9		3.7142	
A.10		4.3332	
A.11		4.9522	
A.12		5.5712	
B.1	90	5.5712	0
B.2			1
B.3			4
B.4			9
B.5			17
B.6			25
B.7			49
B.8			81
C.1			81
C.2			265

The meshing was done with the tools delivered by CFD (Figure 5). In all cases, the meshing was done with the ANSYS automatic marking machine. In case A, hexahedral elements were used, while in Cases B and C, tetrahedral elements were used. The quality of the meshing was verified with the following indicators: Skewness, orthogonal quality, and element quality, and in all three cases, between 75% and 90% of the elements presented a good or superior quality. In addition, the Y-plus was found to be less than 1, indicating that the simulation was sufficiently accurate to represent all the turbulent phenomena in the vicinity of the walls.

The simulations were performed based upon the RSM model. The boundary conditions were based on the experimental conditions (Table 1). A mesh study was performed to assure the mesh non-dependence of the results exposed here (Figure 6 and Table 3).

**Table 3.** Specifications of the mesh used in Cases A, B, and C.

Case	Elements	Fiber Refinement	Specifications
A	Hexahedral	Non	Non-Structured non-conformal mesh
B	Tetrahedra	Yes	Ordering of fibers by angular equidistance
C	Tetrahedra	Yes	Ordering of fibers by triangular tessellation

There were two boundary conditions to be considered (Table 4). Velocity and pressure at the entrance of the geometry were taken from the values shown in Table 2. The pressure at the exit of the module was calculated based on the experimental data [19] expecting a 2% loss of pressure.

**Table 4.** Variable boundary conditions.

Geometry	Boundary Condition	Input Data
Entrance	Velocity inlet	Velocity, Pressure
Exit	Pressure Outlet	Pressure

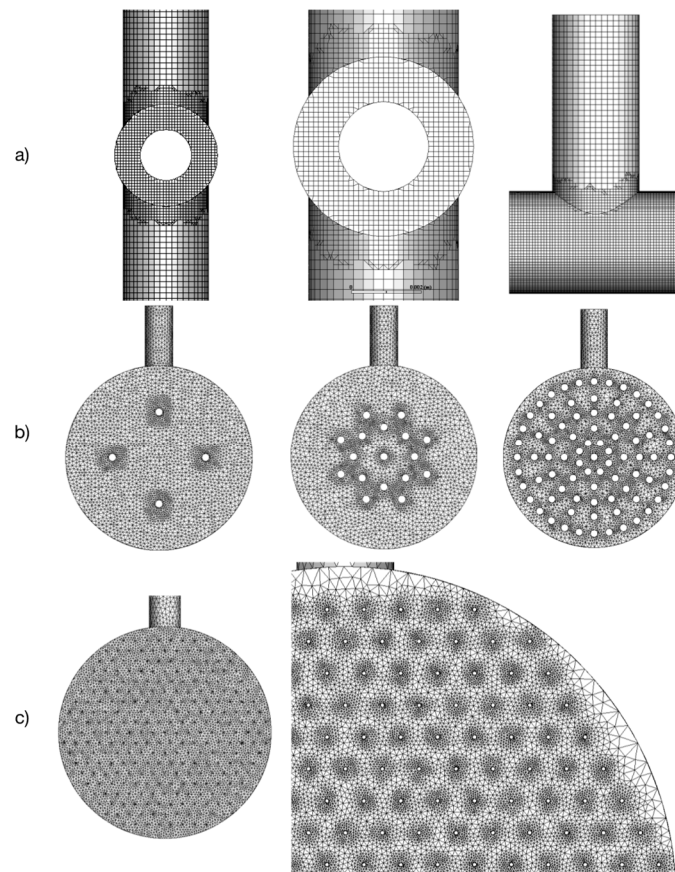


**Figure 6.** Outline of the mesh in Cases A, B, and C. (a) Detail of non-conformal mesh in the critical area of flow entry (experimental), Case A; (b) overview of Case B shows the change in mesh structure when adding more fibers; and (c) overview of Case C by zoom to show the refinement in the fiber vicinity.

### 3. Results

The numerical simulations allowed us to analyze the behavior of the SCF inside the HFMC. Initially, the streamlines were analyzed inside the HFMC in Cases A, B, and C. Then, the development of the velocity profile in the vicinity of the HFMC singularities was verified, as was how this affected the mass transfer.

The streamlines were analyzed because they are indicators of the instantaneous direction of the fluid movement throughout the flow field. Streamlines cannot be directly displayed experimentally, except in steady flow fields where they coincide with the pathlines and streaklines. However, in order to achieve this, one must work with transparent HFMC.

The visualization of the fluid dynamics of fluids in the supercritical state is complex and even more so in small spaces such as in the HFMC; thus, the importance of the results of this research.

#### 3.1. Flow Visualization

Figures 7 and 8 show the streamlines for the HFMC of the experimental conditions studied. In all of these cases, the behavior of an incompressible fluid such as SC-CO<sub>2</sub> was observed. The ratio of linear deformation was positive in the horizontal direction and negative in the vertical one due to the stretching of the fluid element, maintaining the constant volume. Therefore, along with the HFMC, the streamlines tended to approach each other. On the other hand, in all cases, it was observed that in the entrance and the exit of the HFMC, the profile's highest speed was presented. In these curved zones, the viscous resistance reduced the speed in the contour, resulting in the energy being lower there than in the adjacent layers. In addition, it was observed that the lowest system velocity occurred

at the end of the HFMC that was perpendicular to the flow because the SC-CO<sub>2</sub> flows followed the curvature of the streamlines generated at the inlet and outlet of the HFMC. Therefore, one of the first design recommendations is that the HFMC should not have a flat and perpendicular termination at the entrance and exit, but rather the termination should have the shape of the curvature generated by the streamlines.

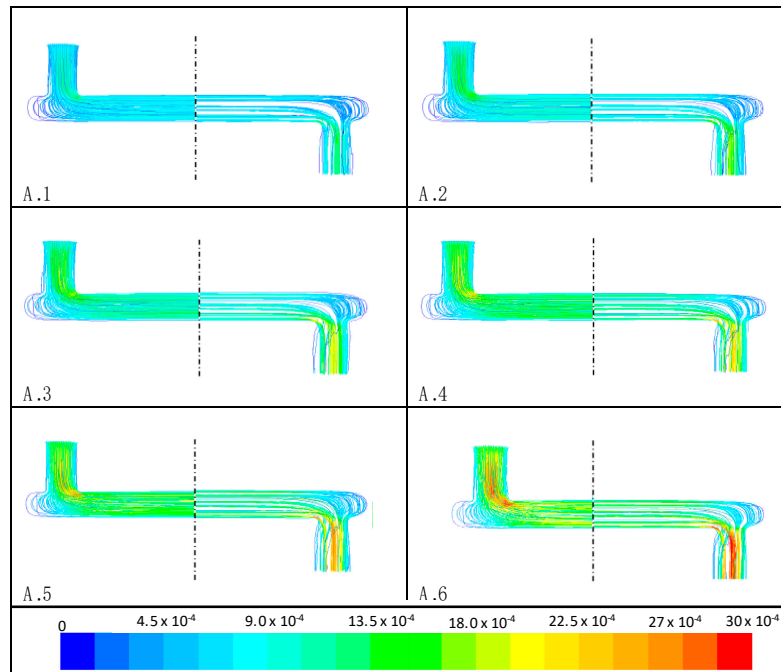


Figure 7. Streamlines of Cases A.1–A.6. Flow direction: Left to right. Velocity in m/s.

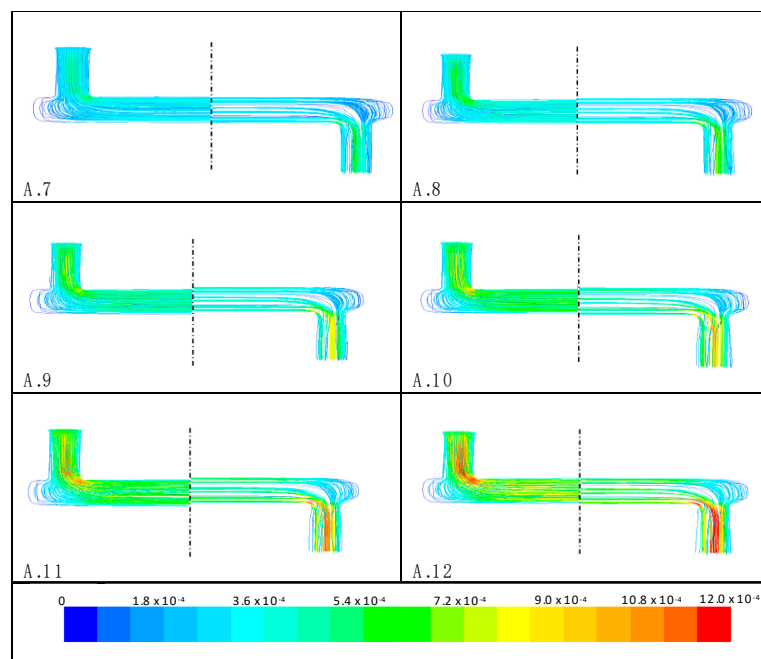


Figure 8. Streamlines of Cases A.7–A.12. Flow from left to right. Velocity in m/s.

In Figures 7 and 8, there are no signs of flow lines forming flow irregularities inside the HFMC, since the available space for the circulation of the SC-CO<sub>2</sub> favored the development of the flow at a short distance from the entrance and exit to the membrane module. In addition, it was observed that

at a pressure of 90 bar, the maximum speed was lower than for the 70 bar. It must be considered that the velocity range was different in both cases since they had the same mass flow. In both of these pressures, the maximum speed value was double the average value.

Figure 9 shows the streamlines in the commercial HFMC. As in the experimental module, velocities of greater magnitude were located at the module’s entrance and exit. The lowest velocity was found around the fibers since this varied according to the conservation of the mass balance.

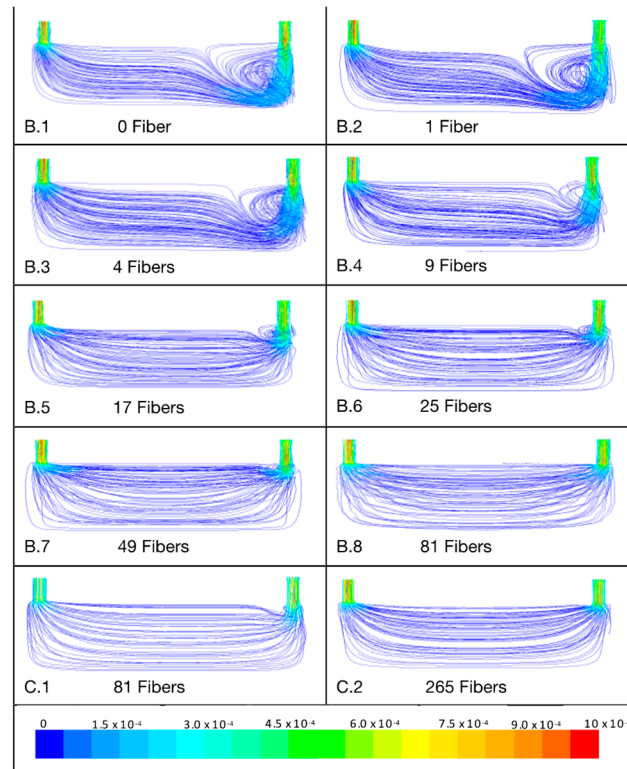
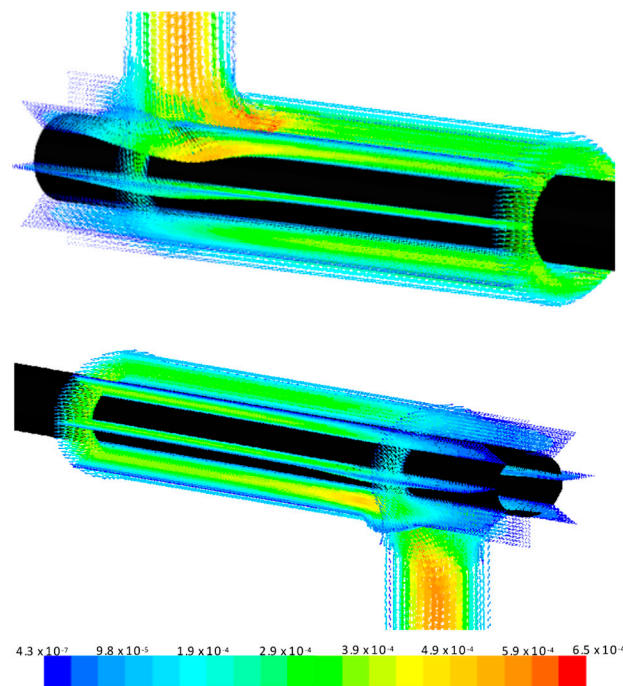


Figure 9. Streamlines of Cases B.1–C.2. Flow from right to left. Velocity in m/s.

On the other hand, it was observed that as the number of fibers increased, the SC-CO<sub>2</sub> recirculation decreased at the entrance of the HFMC. This recirculation occurred due to the abrupt change in the circulation diameter of the SC-CO<sub>2</sub>. Thus, increasing the number of fibers preventing the generation of this recirculation. Due to our limited computational resources for the simulation, it was not possible to increase the number of fibers as well as to reach the actual fiber value of the commercial HFMC, but it was observed that for 265 fibers, the streamlines were parallel and the recirculation of the flow at the entrance did not exist.

In Figure 10, the planes (45°) perpendicular to the fiber of the experimental HFMC can be seen. These planes represent the velocity vectors in the lumen of the experimental HFMC. The velocity had a constant direction 10 mm from the wall of the entrance duct toward the HFMC. The same effect was observed at 10 mm from the SC-CO<sub>2</sub> entry duct. Therefore, this result should be considered when calculating the transport phenomena that depend on the effective area of contact between the fluid and the fiber.

The velocity distribution depends on the geometry of the system, the degree of turbulence, and the nature of the fluid. In a tubular system, the maximum speed is in the axis and the minimum is in the contour. Figure 11 shows the velocity profiles in the fully developed flow region (half of the HFMC). The elongated shape of the parable was due to the fact that since the Reynolds numbers were low, the velocity distribution was very large.



**Figure 10.** Vector representation of velocity (m/s) at the entrance and exit of the membrane (Case A.7). Flow direction: Left to right.

In Figure 11a, the profiles for the experimental HFMC module were observed at 90 bar and the cases at extreme speeds. The parabolic tendency of the curve around the fiber was similar for both speeds. Figure 10b,c represents the velocity profiles for the commercial HFMC. It was observed that the parabolic profile tended to form between the fibers. When comparing Cases B.8 and C.1, the effect of the fiber diameter was observed. For Case B.8 (coarse fiber), it was observed that thinner parabolas than those in Case C.1 (thin fiber) formed between the fibers. When considering the global movement, i.e., summing up all the small parabolas formed between the fibers, the SC-CO<sub>2</sub> did not circulate like a perfect parable but tended rather, to perform a piston-like movement by increasing the number of fibers.

In Table 5, the mean velocity values inside the module that were calculated in the experimental HFMC [19] were compared with those delivered by the numerical simulation. It was observed that the average error was  $0.5 \pm 0.04\%$ , i.e., the results of the simulation were in line with what was expected.

**Table 5.** Comparison of simulated vs. experimental velocity within the HFMC.

Case	Velocity (m/s)		Error
	Experimental	Simulated	
A.1	$6.04 \times 10^{-4}$	$6.01 \times 10^{-4}$	0.504%
A.2	$7.56 \times 10^{-4}$	$7.52 \times 10^{-4}$	0.498%
A.3	$9.07 \times 10^{-4}$	$9.01 \times 10^{-4}$	0.584%
A.4	$1.06 \times 10^{-3}$	$1.05 \times 10^{-3}$	0.547%
A.5	$1.21 \times 10^{-3}$	$1.20 \times 10^{-3}$	0.449%
A.6	$1.36 \times 10^{-3}$	$1.35 \times 10^{-3}$	0.448%
A.7	$2.48 \times 10^{-4}$	$2.46 \times 10^{-4}$	0.490%
A.8	$3.10 \times 10^{-4}$	$3.08 \times 10^{-4}$	0.484%
A.9	$3.71 \times 10^{-4}$	$3.70 \times 10^{-4}$	0.488%
A.10	$4.33 \times 10^{-4}$	$4.31 \times 10^{-4}$	0.492%
A.11	$4.95 \times 10^{-4}$	$4.93 \times 10^{-4}$	0.484%
A.12	$5.57 \times 10^{-4}$	$5.54 \times 10^{-4}$	0.481%

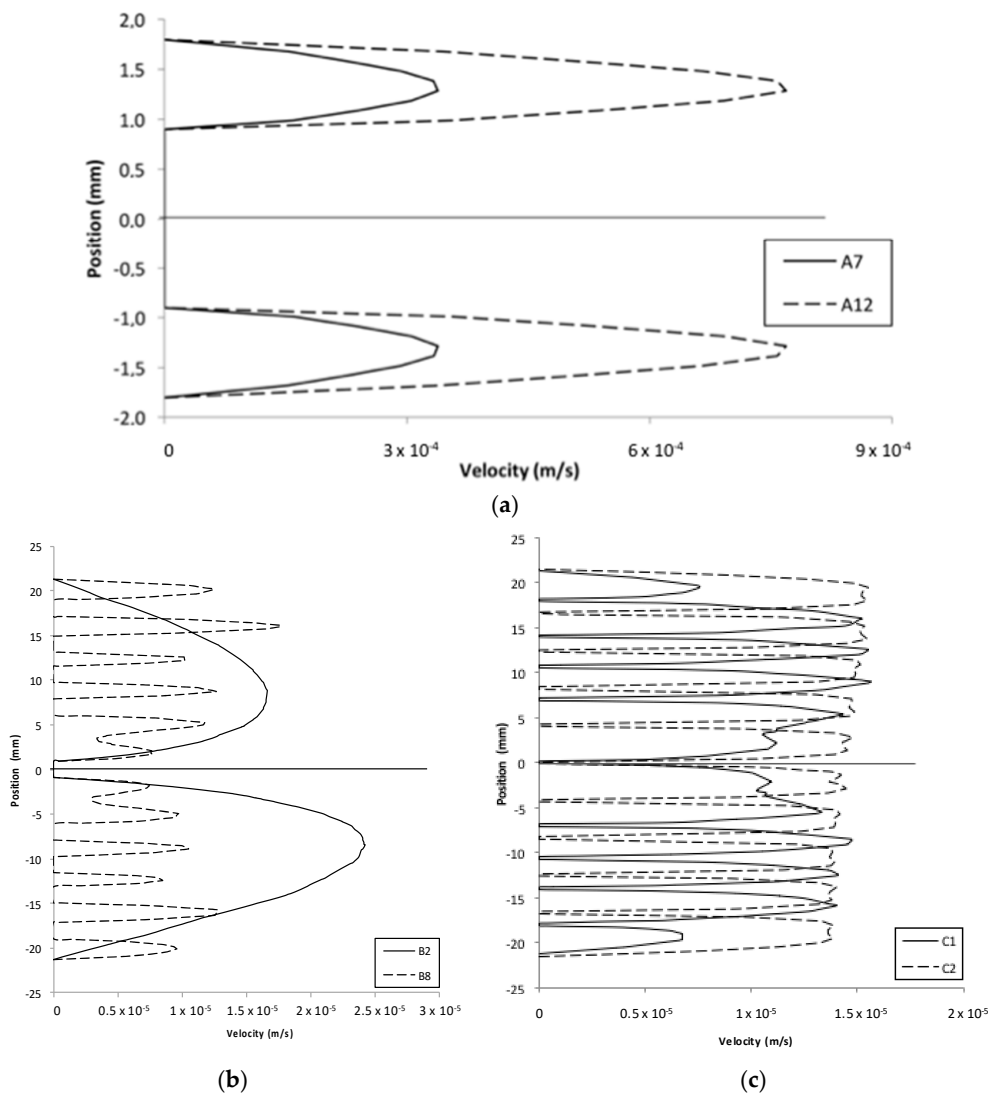


**Figure 11.** Flow developed in Cases (a) A.7 and A.12; (b) B.2 and B.8; and (c) C.1 and C.2.

In Figure 12, it can be observed that the flow was homogeneously distributed in the membrane module as it moved away from the entrance. This corroborated the existence of a “fit” flow section near the entrance.

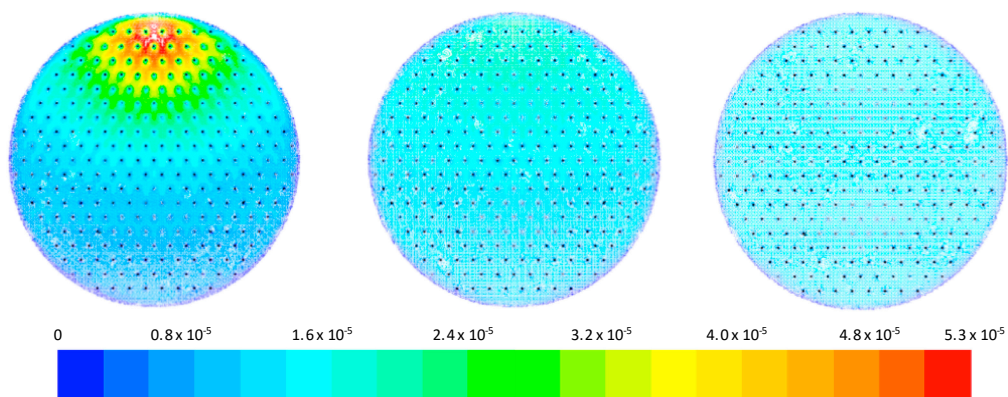


**Figure 12.** Velocity vectors of Case C2 at 15, 30, and 45 mm from the flow entrance.

### 3.2. Profile Development

Figures 13 and 14 show the development of the velocity profile along the HFMC. In the experimental HFMC (Figure 13), a clear tendency was observed, indicating that as the fluid moved along the module, the parabolic profile changed its extension. Thus, in both operating pressures, it was observed that the parabolic profile on the fiber was shortened, while the parabolic profile under the fiber lengthened until both profiles ended up with the same extension.

This is due to the effect that caused the presence of the fiber at the entrance of the SC-CO<sub>2</sub>, toward the commercial HFMC. Consequently, all along the module, that effect was counteracted. In Figure 14, it can be observed that in all four cases, starting at 173 mm from the entry of the fluid, that is, half of the effective length, the profile was kept constant and balanced, whereas, in the commercial HFMC, this equilibrium was achieved at 79% of the effective length.

Figure 14a shows the presence of a velocity profile opposite the flow direction, which confirmed the divergent current lines of Figure 9 (Case B.2). This phenomenon has a very strong effect on the boundary layer since it has the friction effect of the contour. The fluid particles of the boundary layer move very slowly because there is adverse pressure, they start losing speed until they finally stop.

The development of the velocity profile was accompanied by the formation of the boundary layer. For the SC-CO<sub>2</sub> under the simulated conditions, the viscous forces predominated over the inertial forces, therefore, the formation of the boundary layer was facilitated.

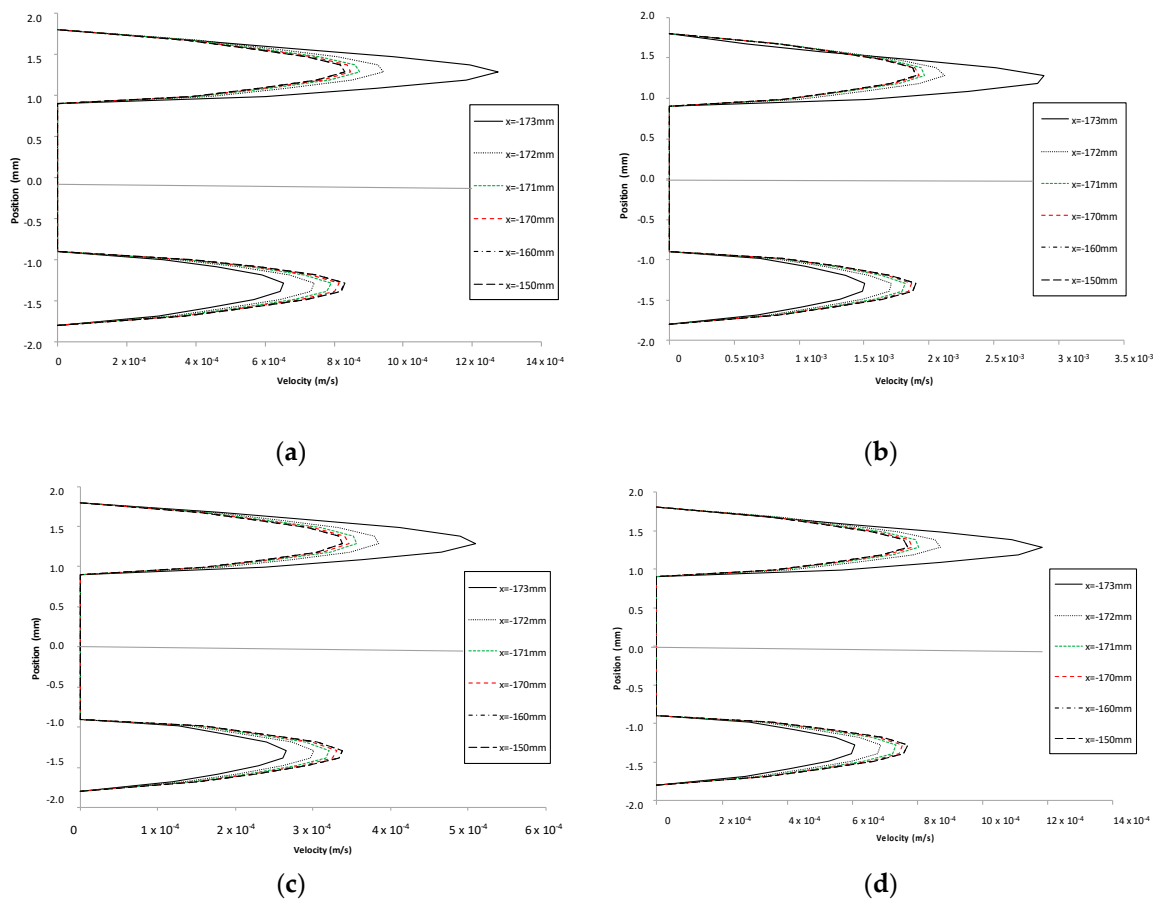


Figure 13. Velocity profile development in Cases (a) A.1; (b) A.6; (c) A.7, and (d) A.12.

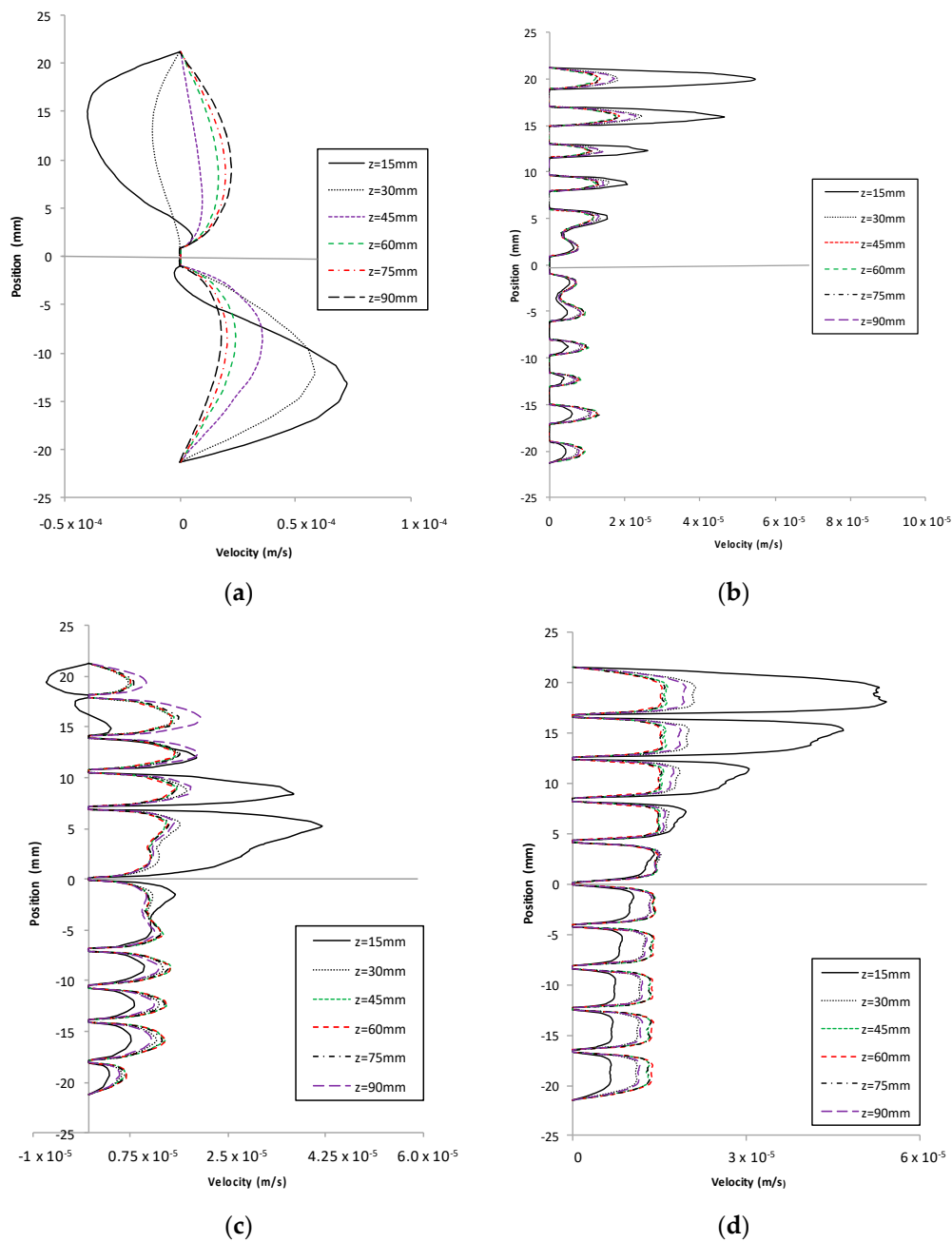


Figure 14. Development of velocity profile, cases (a) B.2, (b) B.8, (c) C.1, and (d) C.2.

### 3.3. Boundary Layer

The influence of the contour is limited to a very thin layer, close to the walls. There, the viscous stresses are large and the velocity gradient is intense. The thickness of the layer is the distance from the contour (velocity = 0) to a point where the velocity of the fluid is velocity in the absence of contour. One way to visualize the boundary layer is with graphs of the vorticity areas (Figure 15).

The fluid particles within the viscous boundary layer are rotational, i.e., they have non-zero vorticity, whereas the fluid particles outside the boundary layer are irrotational, i.e., they have zero vorticity. Thus, in Figure 14, it can be observed that in the central area (blue) of the lumen, there was no vorticity, whereas in the vicinity of the fiber, there was clearly vorticity, and therefore the presence of the boundary layer was confirmed. On the other hand, in Figure 14b, a large presence of vorticity was observed in the entrance and exit towards the commercial HFMC, which was the product of the

expansion and compression, respectively, that the SC-CO<sub>2</sub> was subjected to because of the change in the diameter of the flow area.

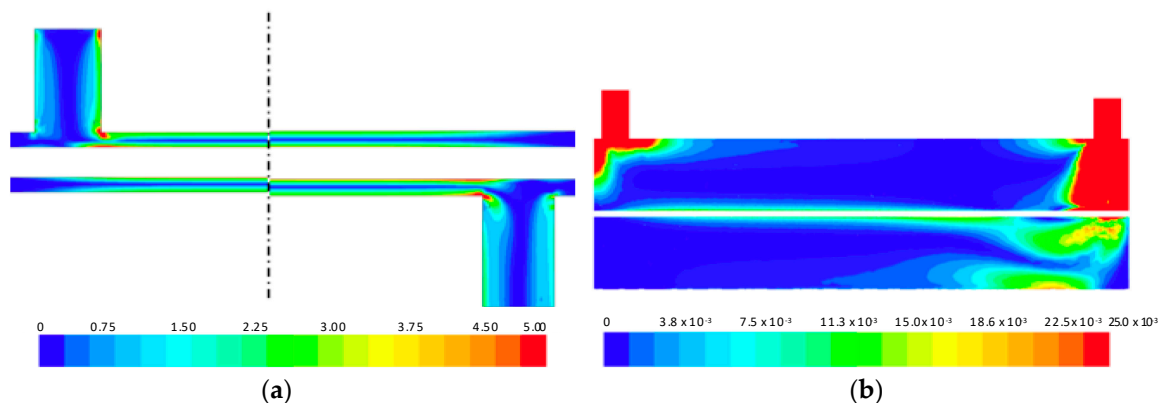


**Figure 15.** Vorticity areas along the HFMC for Cases (a) A.12 (flow direction: Left to right) and (b) B.2 (flow direction: Right to left).

The rotational movement in the boundary layer favors collisions between the particles, which strongly influences the diffusion process. The different-sized molecules have different movements, thus the heavier molecules dominate the diffusion process. On the other hand, it is known that the movement of the fluid considerably improves mass transfer. The Schmidt ( $Sc$ ) number compares the relative magnitudes of the amount of molecular motion and mass diffusion in the velocity and concentration boundary layers, respectively.

In the experimental study [19] that was analyzed with the simulations of this work, the  $Sc$  was between the values 5 and 6, which indicated that the diffusion of momentum in the speed limit layer predominated over the mass diffusion in the boundary layer of concentration, hence, the boundary layers did not exactly match each other. Finally, it is known that the boundary layers are formed in the order: Velocity–thermal–concentration. That is, according to our results, the boundary layer of concentration will form after 10 mm from the wall of the entrance tube of the SC-CO<sub>2</sub> fluid since it is at that distance that the development of the velocity boundary layer was observed.

It is predicted that the exact development of the boundary layer is achieved when the concentration difference between a point on the fiber and the point farthest from the layer is 99% of the difference between the concentration at one point on the fiber and at the fluid circulation center. In order to predict the exact point of the development of the boundary layer, simulations similar to the one carried out in this paper, but applied to the transfer, should be performed, which remains as a projection of this research. The exact definition of the place for the development of the boundary layer would imply an improvement of the simplified models that predict the mass transfer in the HFMC.

#### 4. Discussion

In this research, the Reynolds numbers were very low. Therefore, the turbulent model was used instead of the laminar model as laminar models diverge easily at these speeds.

Research by other authors [1–3,8] has partially described the fluid dynamics inside an HFMC but have focused on the mass transfer and not on the hydrodynamics. In this research, the fluid dynamics inside the HFMC is shown in detail. In this research, the greatest effect on the fluid dynamics of the SC-CO<sub>2</sub> was visualized (3D) along with the changes of the geometry of the module, that is to say, by using different HFMC and by varying the number of fibers. By increasing the number of fibers, the irregularities of the flow at the entrance and at the exit of the HFMC were minimized. Furthermore, “micro-profiles” of velocity between the fibers were produced.

The results showed that the model used fit well with the experimental conditions. It was observed that if there were no changes in the pressure and temperature, as in the experiments of this research, then, the hydrodynamic behavior profile of an SCF was similar to that of a liquid at low pressures.

Polyanin et al. [57] reported the hydrodynamics to underlie numerous processes of chemical engineering science. On the other hand, Pahl and Beitz [58] reported that design is a creative activity that calls for a sound grounding in mathematics, physics, chemistry, mechanics, thermodynamics, hydrodynamics, electrical engineering, production engineering, materials technology, and design theory as well as knowledge and experience of the domain of interest. Therefore, the findings of this research are interesting for technical applications and contribute to the understanding of the hydrodynamics of SCFs.

Future research directions include simulating a membrane module of 5400 fibers or more; using the results of this investigation to estimate the effective area of mass transfer flow; and to consider the hydrodynamic profile throughout the HFMC for new phenomenological models.

## 5. Conclusions

In this research work, the greatest effect on the fluid dynamics of the SC-CO<sub>2</sub> was visualized along with the changes in the geometry of the module by using different HFMC and by varying the number of fibers. By increasing the number of fibers, the irregularities of the flow at the entrance and at the exit of the HFMC were minimized. Furthermore, “micro-profiles” of velocity between the fibers were produced. It was possible to observe different aspects of the fluid dynamics within the HFMC such as current line trends, velocity changes, velocity profile development, boundary layer development, and irregularities, among others. The fluid-dynamic behavior of the SC-CO<sub>2</sub> was dependent on the density, viscosity, velocity, and geometry. Finally, this research answered the question initially asked of what is the fluid dynamic behavior of an SCF inside a membrane module.

**Author Contributions:** Conceptualization, validation, investigation, and writing—original draft preparation, H.V.; methodology, software and writing, K.U.; formal analysis and supervision, A.S.

**Funding:** This research was funded by the Internal Research Project (Universidad Catolica del Maule-434189) with the “Modelación fenomenológica de la remoción de CO<sub>2</sub> con solución carbonatada mediante un contactor de membrana” project, and the APC was funded by the Universidad Catolica del Maule.

**Acknowledgments:** This research is framed within the Internal Research Project (Cod. 434189), funded by Universidad Catolica del Maule, Chile.

**Conflicts of Interest:** The authors declare no conflict of interest.

## References

1. Shirazian, S.; Marjani, A.; Fadaei, F. Supercritical extraction of organic solutes from aqueous solutions by means of membrane contactors: CFD simulation. *Desalination* **2011**, *277*, 135–140. [[CrossRef](#)]
2. Miramini, S.; Razavi, S.; Ghadiri, M.; Mahdavi, S.; Moradi, S. CFD simulation of acetone separation from an aqueous solution using supercritical fluid in a hollow-fiber membrane contactor. *Chem. Eng. Process.* **2013**, *72*, 130–136. [[CrossRef](#)]
3. Ranjbar, M.; Shirazian, S.; Ghafarnejad Parto, S.; Ahmadi, M. Computational fluid dynamics simulation of mass transfer in the separation of fermentation products using nanoporous membranes. *Chem. Eng. Technol.* **2013**, *36*, 728–732. [[CrossRef](#)]
4. Yong, W.F.; Chung, T.S.; Weber, M.; Maletzko, C. New polyethersulfone (PESU) hollow fiber membranes for CO<sub>2</sub> capture. *J. Memb. Sci.* **2018**, *552*, 305–314. [[CrossRef](#)]
5. Pandey, P.; Chauhan, R.S. Membranes for gas separation. *Prog. Polym. Sci.* **2001**, *26*, 853–893. [[CrossRef](#)]
6. Gabelman, A.; Hwang, S.T. Hollow fiber membrane contactors. *J. Memb. Sci.* **1999**, *159*, 61–106. [[CrossRef](#)]
7. Qi, Z.; Cussler, E.L. Microporous hollow fibers for gas absorption: I. Mass transfer in the liquid. *J. Memb. Sci.* **1985**, *23*, 321–332. [[CrossRef](#)]
8. Shirazian, S.; Moghadassi, A.; Moradi, S. Numerical simulation of mass transfer in gas–liquid hollow fiber membrane contactors for laminar flow conditions. *Simul. Model. Pract. Theory* **2009**, *17*, 708–718. [[CrossRef](#)]

9. Li, J.L.; Chen, B.H. Review of CO<sub>2</sub> absorption using chemical solvents in hollow fiber membrane contactors. *Sep. Purif. Technol.* **2005**, *41*, 109–122. [[CrossRef](#)]
10. Pabby, A.K.; Rizvi, S.S.; Requena, A.M.S. *Handbook of Membrane Separations: Chemical, Pharmaceutical, Food, and Biotechnological Applications*; CRC Press: Boca Raton, FL, USA, 2008; ISBN 978-0-8493-9549-9.
11. Brennecke, J.F.; Eckert, C.A. Phase equilibria for supercritical fluid process design. *AIChE J.* **1989**, *35*, 1409–1427. [[CrossRef](#)]
12. Eckert, C.A.; Knutson, B.L.; Debenedetti, P.G. Supercritical fluids as solvents for chemical and materials processing. *Nature* **1996**, *383*, 313. [[CrossRef](#)]
13. Kumar, S.K.; Johnston, K.P. Modelling the solubility of solids in supercritical fluids with density as the independent variable. *J. Supercrit. Fluids* **1988**, *1*, 15–22. [[CrossRef](#)]
14. De Castro, M.D.L.; Valcárcel, M.; Tena, M.T. *Analytical Supercritical Fluid Extraction*; Springer Science & Business Media: Berlin, Germany, 2012; ISBN -13: 978-3-642-78675-4.
15. Engelhardt, H.; Gross, A. Supercritical fluid extraction and chromatography: Potential and limitations. *TrAC Trends Anal. Chem.* **1991**, *10*, 64–70. [[CrossRef](#)]
16. McHugh, M.; Krukonis, V. *Supercritical Fluid Extraction: Principles and Practice*, 2nd ed.; Butterworth-Heinemann; Elsevier: Amsterdam, The Netherlands, 2013; ISBN 0-7506-9244-8.
17. Stephan, K. *Viscosity of Dense Fluids*; Springer Science & Business Media: Berlin, Germany, 2013; ISBN 978-1-4757-6933-3.
18. Brunner, G. *Gas Extraction: An Introduction to Fundamentals of Supercritical Fluids and the Application to Separation Processes*; Springer Science & Business Media: Berlin, Germany, 2013; Volume 4, ISBN 978-3-662-07382-7.
19. Valdés, H.; Sepúlveda, R.; Romero, J.; Valenzuela, F.; Sánchez, J. Near critical and supercritical fluid extraction of Cu (II) from aqueous solutions using a hollow fiber contactor. *Chem. Eng. Process.* **2013**, *65*, 58–67. [[CrossRef](#)]
20. Aminian, A. Estimating the solubility of different solutes in supercritical CO<sub>2</sub> covering a wide range of operating conditions by using neural network models. *J. Supercrit. Fluids* **2017**, *125*, 79–87. [[CrossRef](#)]
21. Baldino, L.; Della Porta, G.; Reverchon, E. Supercritical CO<sub>2</sub> processing strategies for pyrethrins selective extraction. *J. CO<sub>2</sub> Util.* **2017**, *20*, 14–19. [[CrossRef](#)]
22. García-Pérez, J.S.; Robledo-Padilla, F.; Cuellar-Bermudez, S.P.; Arévalo-Gallegos, A.; Parra-Saldivar, R.; Zavala-Yoe, R.; Ramírez-Mendoza, R.; Iqbal, H.M. Thermodynamics and statistical correlation between supercritical-CO<sub>2</sub> fluid extraction and bioactivity profile of locally available Mexican plants extracts. *J. Supercrit. Fluids* **2017**, *122*, 27–34. [[CrossRef](#)]
23. Rezzadori, K.; Penha, F.M.; Prando, L.T.; Zin, G.; Friedrich, M.T.; Di Luccio, M.; Petrus, J.C.C. Characterization and performance of reverse osmosis and nanofiltration membranes submitted to subcritical and supercritical CO<sub>2</sub>. *J. Supercrit. Fluids* **2017**, *128*, 39–46. [[CrossRef](#)]
24. Leybros, A.; Hung, L.; Hertz, A.; Hartmann, D.; Grandjean, A.; Boutin, O. Supercritical CO<sub>2</sub> extraction of uranium from natural ore using organophosphorus extractants. *Chem. Eng. J.* **2017**, *316*, 196–203. [[CrossRef](#)]
25. Babova, O.; Occhipinti, A.; Capuzzo, A.; Maffei, M.E. Extraction of bilberry (*Vaccinium myrtillus*) antioxidants using supercritical/subcritical CO<sub>2</sub> and ethanol as co-solvent. *J. Supercrit. Fluids* **2016**, *107*, 358–363. [[CrossRef](#)]
26. Reverchon, E.; Marrone, C. Modeling and simulation of the supercritical CO<sub>2</sub> extraction of vegetable oils. *J. Supercrit. Fluids* **2001**, *19*, 161–175. [[CrossRef](#)]
27. Sánchez-Vicente, Y.; Cabañas, A.; Renuncio, J.A.; Pando, C. Supercritical fluid extraction of peach (*Prunus persica*) seed oil using carbon dioxide and ethanol. *J. Supercrit. Fluids* **2009**, *49*, 167–173. [[CrossRef](#)]
28. Duba, K.S.; Fiori, L. Solubility of grape seed oil in supercritical CO<sub>2</sub>: Experiments and modeling. *J. Chem. Thermodyn.* **2016**, *100*, 44–52. [[CrossRef](#)]
29. Valdés, H. Extracción con Fluidos Supercríticos de Metales a Partir de Soluciones Acuósas Utilizando un Contactor de Membrana de Fibra Hueca. Ph.D. Thesis, Universidad de Santiago de Chile, Santiago, Chile, 2010.
30. Pabby, A.K.; Sastre, A.M. State-of-the-art review on hollow fiber contactor technology and membrane-based extraction processes. *J. Memb. Sci.* **2013**, *430*, 263–303. [[CrossRef](#)]
31. Brogle, H. CO<sub>2</sub> as a solvent: Its properties and applications. *Chem. Ind.* **1982**, 385–390.

32. Stahl, E.; Gerard, D. Solubility behaviour and fractionation of essential oils in dense carbon dioxide. *Perfum. Flavor* **1985**, *10*, 29–36.
33. Robinson, J.; Sims, M.U.S. Method and system for extracting a solute from a fluid using dense gas and a porous membrane, Patent N°5,490,884. U.S. Patent and Trademark Office: Washington, DC, USA, 1996.
34. Sarrade, S.; Guizard, C.; Rios, G.M. New applications of supercritical fluids and supercritical fluids processes in separation. *Sep. Purif. Technol.* **2003**, *32*, 57–63. [[CrossRef](#)]
35. Sarrade, S.; Guizard, C.; Rios, G.M. Membrane technology and supercritical fluids: Chemical engineering for coupled processes. *Desalination* **2002**, *144*, 137–142. [[CrossRef](#)]
36. Baldino, L.; Cardea, S.; Reverchon, E. Optimization of HYAFF Membranes Morphology Produced by Supercritical Phase Separation for Biomedical Applications. *Chem. Eng.* **2017**, *57*. [[CrossRef](#)]
37. Gabelman, A.; Hwang, S.T.; Krantz, W.B. Dense gas extraction using a hollow fiber membrane contactor: Experimental results versus model predictions. *J. Memb. Sci.* **2005**, *257*, 11–36. [[CrossRef](#)]
38. Shamu, A.; Miedema, H.; Borneman, Z.; Nijmeijer, K. Permeation of supercritical CO<sub>2</sub> through dense polymeric membranes. *J. Supercrit. Fluids* **2018**, *144*, 63–70. [[CrossRef](#)]
39. Gonçalves, L.M.; Valente, I.M.; Rodrigues, J.A. Recent advances in membrane-aided extraction and separation for analytical purposes. *Sep. Purif. Rev.* **2017**, *46*, 179–194. [[CrossRef](#)]
40. Bothun, G.D.; Knutson, B.L.; Strobel, H.J.; Nokes, S.E. Mass transfer in hollow fiber membrane contactor extraction using compressed solvents. *J. Memb. Sci.* **2003**, *227*, 183–196. [[CrossRef](#)]
41. Moreno, T.; Tallon, S.J.; Catchpole, O.J. Supercritical CO<sub>2</sub> Extraction of 1-Butanol and Acetone from Aqueous Solutions Using a Hollow-Fiber Membrane Contactor. *Chem. Eng. Technol.* **2014**, *37*, 1861–1872. [[CrossRef](#)]
42. Sepúlveda, R.; Romero, J.; Sánchez, J. Copper removal from aqueous solutions by means of ionic liquids containing a  $\beta$ -diketone and the recovery of metal complexes by supercritical fluid extraction. *J. Chem. Technol. Biotechnol.* **2014**, *89*, 899–908. [[CrossRef](#)]
43. Ghadiri, M.; Asadollahzadeh, M.; Hemmati, A. CFD simulation for separation of ion from wastewater in a membrane contactor. *J. Water Process Eng.* **2015**, *144*–150. [[CrossRef](#)]
44. Valdés, H.; Romero, J.; Saavedra, A.; Plaza, A.; Bubnovich, V. Concentration of noni juice by means of osmotic distillation. *J. Membr. Sci.* **2009**, *330*, 205–213. [[CrossRef](#)]
45. Valdés, H.; Romero, J.; Sanchez, J.; Bocquet, S.; Rios, G.M.; Valenzuela, F. Characterization of chemical kinetics in membrane-based liquid–liquid extraction of molybdenum (VI) from aqueous solutions. *Chem. Eng. J.* **2009**, *151*, 333–341. [[CrossRef](#)]
46. Estay, H.; Ortiz, M.; Romero, J. A novel process based on gas filled membrane absorption to recover cyanide in gold mining. *Hydrometallurgy* **2013**, *134*, 166–176. [[CrossRef](#)]
47. Qi, Z.; Cussler, E.L. Microporous hollow fibers for gas absorption: II. Mass transfer across the membrane. *J. Membr. Sci.* **1985**, *23*, 333–345. [[CrossRef](#)]
48. Ghadiri, M.; Shirazian, S.; Ashrafizadeh, S.N. Mass transfer simulation of gold extraction in membrane extractors. *Chem. Eng. Technol.* **2012**, *35*, 2177–2182. [[CrossRef](#)]
49. Shen, S.; Kentish, S.E.; Stevens, G.W. Shell-side mass-transfer performance in hollow-fiber membrane contactors. *Solvent Extr. Ion Exch.* **2010**, *28*, 817–844. [[CrossRef](#)]
50. Romero, J.; Rios, G.M.; Sanchez, J.; Saavedra, A. Analysis of boundary layer and solute transport in osmotic evaporation. *AIChE J.* **2003**, *49*, 2783–2792. [[CrossRef](#)]
51. Estay, H.; Bocquet, S.; Romero, J.; Sanchez, J.; Rios, G.M.; Valenzuela, F. Modeling and simulation of mass transfer in near-critical extraction using a hollow fiber membrane contactor. *Chem. Eng. Sci.* **2007**, *62*, 5794–5808. [[CrossRef](#)]
52. Bocquet, S.; Romero, J.; Sanchez, J.; Rios, G.M. Membrane contactors for the extraction process with subcritical carbon dioxide or propane: Simulation of the influence of operating parameters. *J. Supercrit. fluids* **2007**, *41*, 246–256. [[CrossRef](#)]
53. Vyhmeister, E.; Estay, H.; Romero, J.; Cubillos, F. Simulation and process optimization of a membrane-based dense gas extraction using hollow fiber contactors. *Chem. Eng. Commun.* **2012**, *199*, 644–657. [[CrossRef](#)]
54. Rhie, C.M.; Chow, W.L. Numerical study of the turbulent flow past an airfoil with trailing edge separation. *AIAA J.* **1983**, *21*, 1525–1532. [[CrossRef](#)]
55. Ferziger, J.H.; Perić, M. *Computational Methods for Fluid Dynamics*; Springer: Berlin, Germany, 2002.
56. Patel, V.C.; Rodi, W.; Scheuerer, G. Turbulence models for near-wall and low Reynolds number flows—A review. *AIAA J.* **1985**, *23*, 1308–1319. [[CrossRef](#)]

57. Polyenin, A.D.; Kutepov, A.M.; Kazenin, D.A.; Vyazmin, A.V. *Hydrodynamics, Mass and Heat Transfer in Chemical Engineering*; CRC Press: Boca Raton, FL, USA, 2001; ISBN 978-1-4200-2451-7.
58. Pahl, G.; Beitz, W. *Engineering Design: A Systematic Approach*; Springer Science & Business Media: Berlin, Germany, 2013.



© 2019 by the authors. Licensee MDPI, Basel, Switzerland. This article is an open access article distributed under the terms and conditions of the Creative Commons Attribution (CC BY) license (<http://creativecommons.org/licenses/by/4.0/>).